Magnetotransport mechanisms and magnetoresistive properties in La0.75Dy0.05Sr0.2MnO3 polycrystalline manganite

A. Elghoul, A. Krichene, Nassira Boudjada, F. Fettar, F. Gay, W. Boujelben

Magnetotransport mechanisms and magnetoresistive properties in $La_{0.75}Dy_{0.05}Sr_{0.2}MnO_3$ polycrystalline manganite

A. Elghoul, A. Krichene, N. Chniba Boudjada, F. Fettar, F. Gay & W. Boujelben

Journal of Materials Science: Materials in Electronics

ISSN 0957-4522

J Mater Sci: Mater Electron
DOI 10.1007/s10854-020-03277-y

Springer

Journal of Materials Science: Materials in Electronics
https://doi.org/10.1007/s10854-020-03277-y

Magnetotransport mechanisms and magnetoresistive properties in $La_{0.75}Dy_{0.05}Sr_{0.2}MnO_3$ polycrystalline manganite

A. Elghoul[1] · A. Krichene[1] · N. Chniba Boudjada[1,2] · F. Fettar[2] · F. Gay[2] · W. Boujelben[1]

Received: 15 February 2020 / Accepted: 19 March 2020

Abstract
We have studied in this work the electrical and magnetoresistive properties of polycrystalline $La_{0.75}Dy_{0.05}Sr_{0.2}MnO_3$. Magnetic study has shown the presence of a paramagnetic–ferromagnetic transition at Curie temperature $T_C = 225$ K. Temperature-dependent resistivity shows two resistivity peaks. The magnetotransport in the metallic phase can be described by Zener's polynomial law, while small polaron hopping mechanism is more suitable to describe resistivity evolution in the insulating phase. The resistivity upturn observed around 75 K was ascribed to electron–electron scattering process at low temperature. We have recorded important values of negative magnetoresistance (MR) around T_C (MR $(T) \sim 22\%$ and MR $(H) \sim 19\%$) for only 1 T applied magnetic field. This suggests the possibility of using our sample for magnetic field sensing and spintronics.

1 Introduction

The perovskite manganites $R_{1-x}A_xMnO_3$ (R = rare earth ions and A = alkaline earth ions) have attracted intense research activities in recent years due to their important structural, magnetic and transport properties [1–8]. These compounds possess a wide range of technological applications such as magnetic field sensing, data storage, and magnetic refrigeration. They are also characterized by interesting magnetotransport properties as well as the colossal magnetoresistance (MR) phenomenon defined as a sharp decrease of the electrical resistivity under applied magnetic field, which is very useful for spintronic applications [9, 10]. Several studies have indicated that phase separation plays a key role in the physics of manganites [11–13], which is a direct result of the percolative nature of the metal–insulator transition [14].

Dysprosium is a rare earth element characterized by important magnetic properties. In fact, Dy^{3+} ions possess a high magnetic moment value ($\sim 10.6\ \mu_B$). This fact indicates that the substitution by Dy in manganites, even using small amounts, will highly affect structural, magnetic and electrical response of these compounds [15–18].

Previous studies have been carried out on the sample $La_{0.75}Dy_{0.05}Sr_{0.2}MnO_3$ (LDSMO) [15, 16]. Studies have revealed that LDSMO compound is single-phased and crystallizes in the orthorhombic structure with *Pnma* space group. Besides, the partial substitution of La^{3+} ($r_A = 1.216$ Å) by smaller Dy^{3+} ions ($r_A = 1.083$ Å) in $La_{0.8}Sr_{0.2}MnO_3$ leads to a decrease of the volume per formula unit (V/f.u) from 59.125 to 59.069 $Å^3$ [15]. Moreover, such substitution reduces the average ionic radius at A-site from 1.235 Å to 1.228 Å and highly enhances the cationic mismatch σ^2 from $14.13 \times 10^{-4} Å^2$ to 25.04×10^{-4} $Å^2$. The magnetic study has revealed that our sample exhibits a ferromagnetic–paramagnetic transition with increasing temperature at $T_C = 225$ K. Our results have shown that LDSMO compound has a large value of magnetocaloric effect and high relative cooling power (RCP) (RCP = 96 J/kg for 2 T applied field). In addition, we have previously studied the effect of rare earth substitution effect on the magnetic interactions in $La_{0.75}R_{0.05}Sr_{0.2}MnO_3$ (R = La, Eu, Sm, Gd, Dy and Ho) and the theoretical studies has shown an exception for Dy substitution [16]. In fact, all the $La_{0.75}R_{0.05}Sr_{0.2}MnO_3$ (R = La, Eu, Sm, Gd and Ho) compounds belong to the 3D Ising universality class. However, the substitution by Dy ions changes the universality class from 3D Ising to tricritical mean field, which can be attributed to the intrinsic contribution of Dy^{3+} ions [16]. Thus, we expected that this sample may exhibit interesting magnetotransport properties. In this paper, we are interested to study

✉ A. Krichene
akramkri@hotmail.fr

[1] Laboratoire de Physique Des Matériaux, Faculté Des Sciences de Sfax, Université de Sfax, B.P. 1171, 3000 Sfax, Tunisia

[2] Université Grenoble Alpes, CNRS, Grenoble INP, Institut Néel, 38000 Grenoble, France

Published online: 04 April 2020

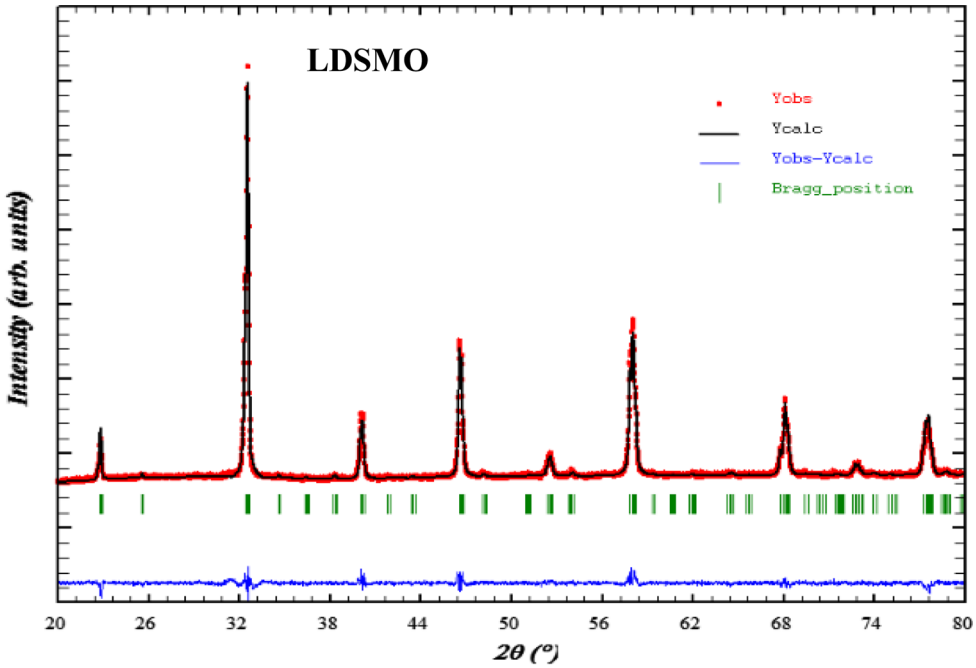

Fig. 1 Rietveld fitted XRD pattern of LDSMO compound

the electrical and the magnetotransport properties of LDSMO compound.

2 Experimental techniques

Polycrystalline LDSMO sample was prepared by sol–gel technique by using high-purity (99.9%) La_2O_3, Dy_2O_3, $SrCO_3$ and MnO_3 (Sigma Aldrich). The synthesis procedure was previously described [15]. X-ray diffraction (XRD) pattern was recorded using Panalytical X'Pert PRO diffractometer with a Philips PW3050/60 X-ray generator (CuKα radiation, $\lambda = 1.5418$ Å). The chemical composition and the morphology of our sample were studied using a JEOL 840 A Scanning electron microscope (SEM). Resistivity measurements were carried out in the temperature range 50–293 K using a Physical Property Measurement System (PPMS, Quantum Design) with applied magnetic field values up to 2 T. The magnetic measurements were carried out using a vibrating sample magnetometer (BS2 VSM) under magnetic field values up to 7 T in the temperature range 5–330 K.

3 Results and discussion

The XRD pattern for LDSMO sample is shown in Fig. 1. Rietveld refinement of the XRD data using FULLPROOF software indicates that the sample is single-phased and crystallizes in the orthorhombic structure with *Pnma* space group with a unit cell volume equal to 236.28 $Å^3$ [15]. The Goodness of fit χ^2 is about 2.47, testifying the fitting quality.

Figure 2 shows a SEM photograph of LDSMO compound. The SEM image shows the presence of composition heterogeneity (black and white), with the presence of sintering neck between particles, which can enhance the connectivity and the electrical conductivity between grains, leading to a reduction of scattering mechanisms. From the SEM image, we have evaluated the average grain size, which is around 0.7 µm. In addition, energy-dispersive X-ray (EDX), as shown in Fig. 3, confirms the presence of La, Dy, Sr, Mn and O elements, as well as the purity of the obtained compound due to the absence of other elements.

Figure 4 shows the temperature-dependent field-cooled (FC) and zero field-cooled (ZFC) magnetization at 0.05 T applied field for LDSMO sample. The curve shows a paramagnetic–ferromagnetic transition when the temperature decreases for our sample. The Curie temperature T_C is

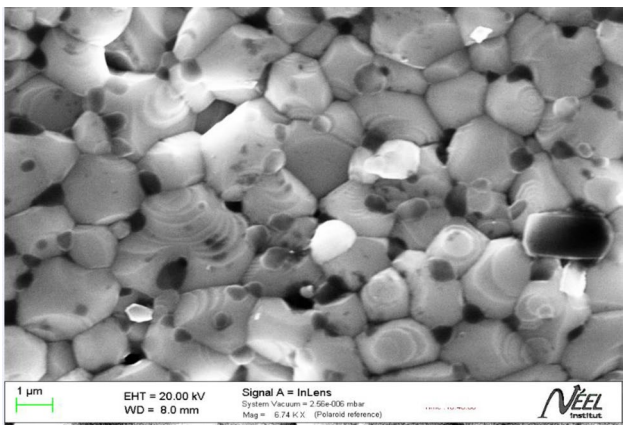

Fig. 2 SEM image of LDSMO compound

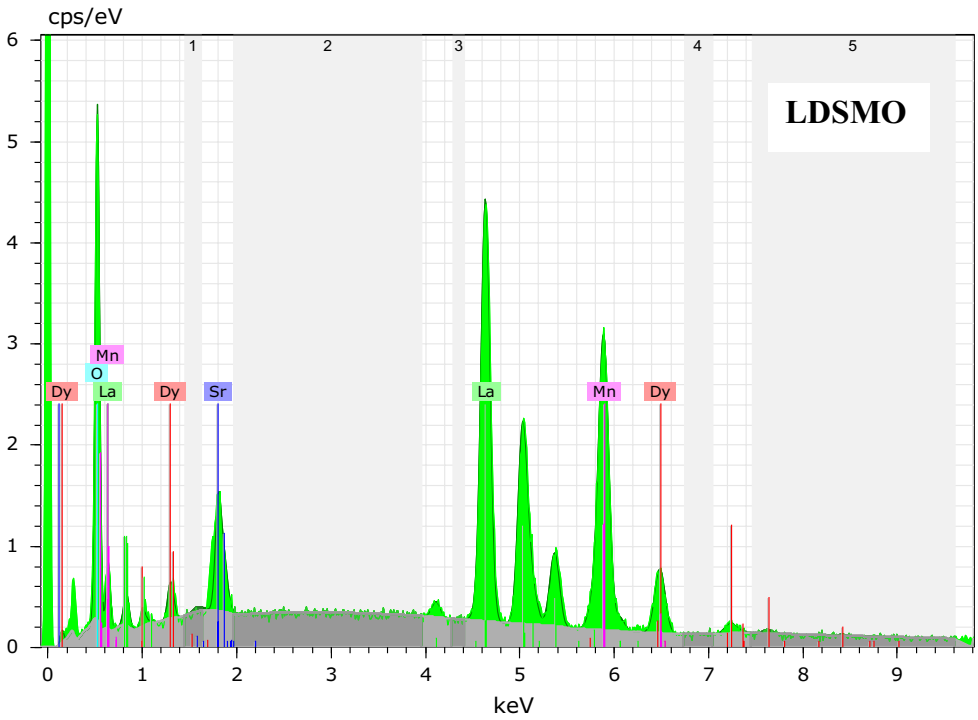

Fig. 3 Energy-dispersive X-ray of LDSMO compound

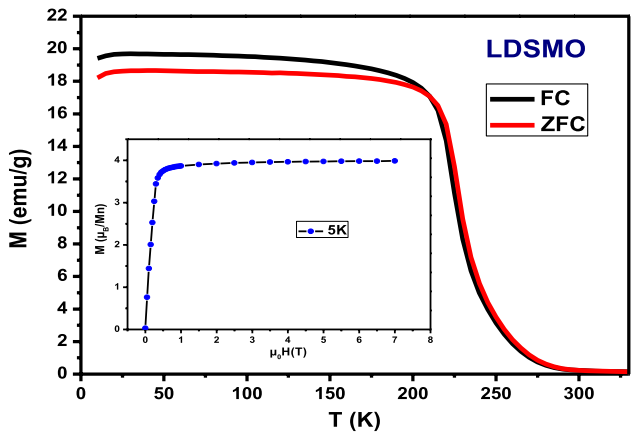

Fig. 4 Temperature dependence of magnetization of LDSMO sample under an applied magnetic field of 0.05 T [15]. The inset shows the magnetic field dependence of the magnetization at 5 K

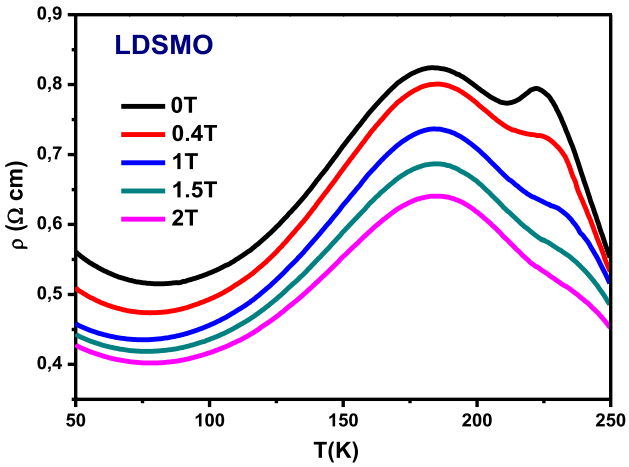

Fig. 5 Temperature dependence of electrical resistivity for several values of applied magnetic field for LDSMO compound

around 225 K (calculated from the minimum of the dM/dT vs.T curve). Both FC and ZFC curves are separated below the magnetic transition, which suggests that the ferromagnetic phase is not homogenous. We have plotted in the inset of Fig. 4 the magnetization variation versus magnetic applied field at 5 K for LDSMO compound. It is obvious that the value of experimental saturation magnetization ($M_{sat}^{exp} = 4\ \mu_B$/Mn) is greater than the theoretical value of saturation magnetization expected for our sample ($M_{sat}^{th} = 3.8\ \mu_B$/Mn) which is calculated by considering only the magnetic moment of manganese ions with a full spin alignment. Thus, this result can be explained by the contribution of dysprosium ions Dy^{3+} which possess an important magnetic moment (10.6 μ_B/Mn), which can be aligned according to the magnetic field direction and thus contribute to experimental saturation magnetization.

To study the magnetotransport properties of LDSMO sample, the evolution of resistivity as a function of temperature for several values of applied magnetic field up to 2 T is shown in Fig. 5. It is clear that LDSMO sample exhibits a metal–insulator transition with increasing temperature around $T_\rho = 180$ K for different applied magnetic field. In the presence

of an applied field, the resistivity decreases, and T_ρ slightly shifts to higher values, from 180 K in zero field to 185 K in 2 T field. This suggests that the applied magnetic field facilitates the hopping of e_g electrons between neighboring Mn ions, which agrees with the double exchange model. The zero and 0.4 T field resistivity curves for LDSMO sample show a second resistivity peak around Curie temperature $T_C = 225$ K. The higher temperature transition recorded near T_C is usually described as the metal–insulator transition due to grain effects (intrinsic effect) that arises due to the competition between double exchange and super exchange mechanisms. This fact is confirmed by the occurrence of this transition in the vicinity of the magnetic transition at T_C. The lower temperature transition (T_ρ) can be related to the contribution of grain boundaries effects (extrinsic effect). Previous works have also shown that the broad transition at the low-temperature $T_{\rho 1}$ presents a higher magnitude than the sharp transition at high-temperature $T_{\rho 2}$, which is consistent with our result [19–22]. It can be seen that, the applied field (for $\mu_0 H \geq 1$ T) suppressed the resistivity peak located near T_C. This fact suggests that the magnetic field enhances the hopping of e_g electrons, which tips the balance in favor of ferromagnetic metallic tendencies. We have also noticed the presence of an insulating behavior below 75 K and its origin will be discussed later. To understand the nature of conduction mechanism below T_ρ in the temperature range 90–160 K, resistivity data in the metallic region for different applied magnetic field values for LDSMO sample were fitted according to the following equation:

$$\rho = \rho_0 + \rho_2 T^2 + \rho_{4.5} T^{4.5} \quad (1)$$

where ρ_0 is the temperature-independent residual resistivity due to scattering by impurities, defects, grain boundaries and domain walls. The second term $\rho_2 T^2$ is ascribed to the electron–electron scattering mechanism, and the third term $\rho_{4.5} T^{4.5}$ is a combination of electron–electron, electron–magnon and electron–phonon scattering processes. The fitted curves are shown in Fig. 6 and the obtained parameters are summarized in Table 1. The ρ_0 and $\rho_{4.5}$ parameters are found to decrease continuously with increasing of the applied magnetic fields. This result can be due to decrease of scattering mechanisms due to the presence of magnetic field. We have previously indicated the presence of a resistivity minimum near 75 K. Resistivity behavior in the vicinity of 75 K can be described using the following relation:

$$\rho = \alpha - \beta\sqrt{T} + \gamma T^n \quad (2)$$

where α is the residual resistivity, $\beta\sqrt{T}$ term describes the electron–electron coulombic elastic interactions and γT^n term refers to inelastic scattering processes. It is obvious from Fig. 7 that relation (**2**) is in agreement with

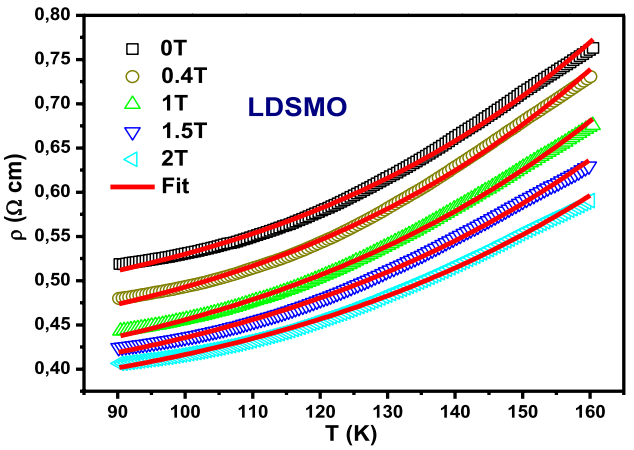

Fig. 6 Temperature dependence of electrical resistivity in the metallic phase under several values of applied magnetic field for LDSMO sample. The line represents the fitting according to relation (1)

Table 1 Fitting parameters in the metallic region and around resistivity minimum under several values of applied magnetic field for LDSMO sample

$\mu_0 H$ (T)	0	0.4	1	1.5	2
ρ_0 (Ω cm)	0.453	0.412	0.372	0.362	0.351
ρ_2 (10^{-6} Ω cm K^{-2})	5.695	6.025	6.730	5.809	5.185
$\rho_{4.5}$ (10^{-11} Ω cm $K^{-4.5}$)	2.067	2.085	1.641	1.519	1.360
T_{min} (K)	75	80	77	79	80
α (Ω cm)	1.081	0.983	0.771	0.753	0.749
β (10^{-2} Ω cm $K^{-0.5}$)	8.344	7.694	4.926	4.886	5.112
γ (10^{-6} Ω cm K^{-n})	25.005	29.340	3.891	4.476	8.372
n	2.026	1.991	2.330	2.282	2.164

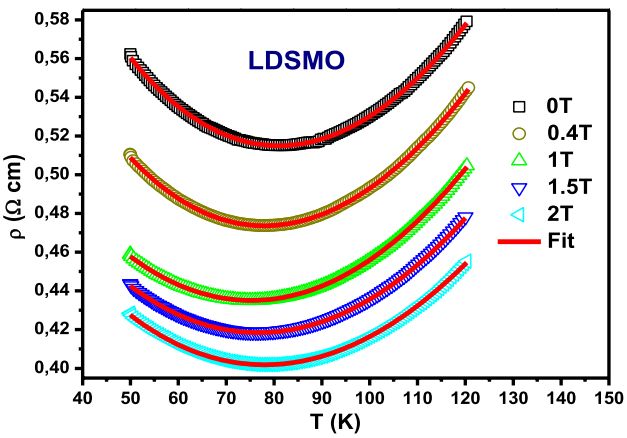

Fig. 7 Temperature dependence of electrical resistivity in vicinity of resistivity minimum under several values of applied magnetic field for LDSMO sample. The line represents the fitting according to relation (2)

experimental data. The best fitting results for our sample in the temperature range 50–120 K are given in Table 1. The low-temperature resistivity upturn characterizes several manganites [17, 23–28]. We can see that α and β parameters decrease with field application. For residual resistivity α, the decrease with applied magnetic field can be attributed to the enhancement of double exchange and, hence, decrease in electrical resistivity. The decrease of β parameter indicates a reduction of minima depth due to the field-induced suppression of elastic scattering mechanisms. For $\mu_0 H \geq 1$ T, γ coefficient increases, indicating an enhancement of inelastic scattering processes. The n exponent is near to 2 for all applied magnetic fields, which is a characteristic of electron–electron interactions.

The evolution of resistivity at higher temperatures $T > T_\rho$ can be described by three models: the small polaron hopping (SPH) model, the variable-range hopping (VRH) model and thermal activation (TA) model. For SPH model, the thermal energy is sufficient to allow the electrons hopping to the nearest neighbors by multiphonon-assisted process. This mechanism is described by the following relation:

$$\rho = \rho_0 T \exp\left(\frac{E_a}{k_B T}\right) \tag{3}$$

where E_a is the hopping energy, ρ_0 is a constant and k_B is the Boltzmann constant. The hopping activation energy can be estimated from slope of the In(ρ) versus 1/T curve as displayed in Fig. 8. Values of ρ_0 and E_a are given in Table 2. It is interesting to note that values of ρ_0 and E_a increase and decrease, respectively, with increasing the magnetic field. The VRH model describes the hopping of a charge carrier from a localized state to another; this model can also describe the evolution of resistivity above T_C (Fig. 9), and this law can be written as follows:

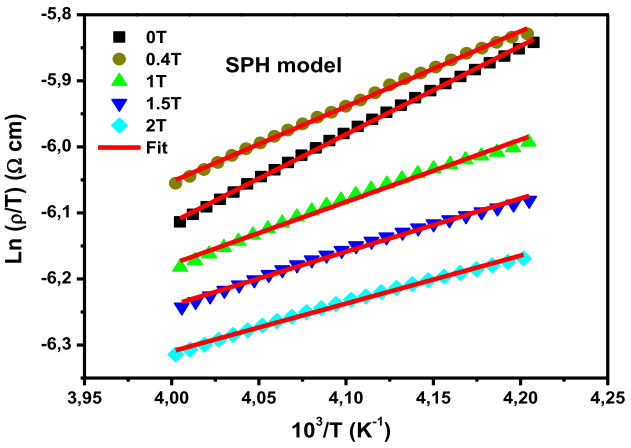

Fig. 8 Fit of high-temperature resistivity data using SPH model for LDSMO sample

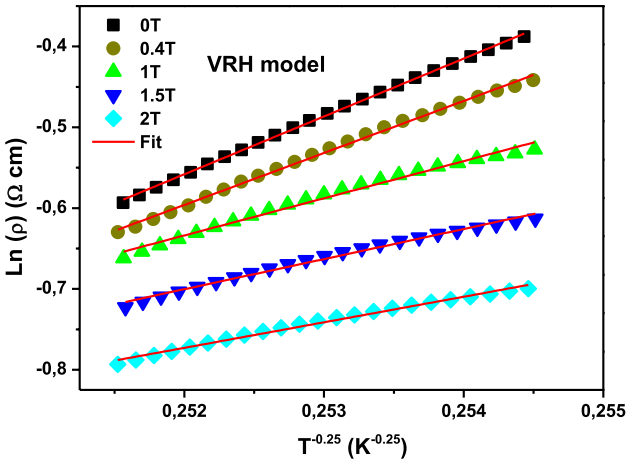

Fig. 9 Fit of high-temperature resistivity data using VRH model for LDSMO sample

Table 2 Resistivity fitting parameters in the insulating region under several values of applied magnetic field for LDSMO sample

$\mu_0 H$ (T)	0	0.4	1	1.5	2
SPH					
ρ_0 (10^{-5}Ω cm K^{-1})	1.051	2.472	4.796	7.691	10.024
E_a (mev)	115.23	98.14	81.17	69.65	62.40
R^2	0.999	0.998	0.992	0.994	0.995
VRH					
ρ_0 (Ω cm)	8.4710^{-9}	5.0210^{-8}	4.9110^{-6}	4.1810^{-5}	1.6010^{-4}
T_0 (10^6 K)	26.19	17.13	4.48	1.92	0.99
$N(E_F)$ (10^{10} eV^{-1} m^{-3})	0.303	0.463	1.769	4.123	8.038
R^2	0.999	0.997	0.987	0.990	0.991
TA					
ρ_0 (10^{-2} Ω cm)	0.696	1.044	3.177	5.095	6.645
E_a (mev)	94.23	84.75	60.17	48.66	41.43
R^2	0.999	0.996	0.986	0.988	0.989

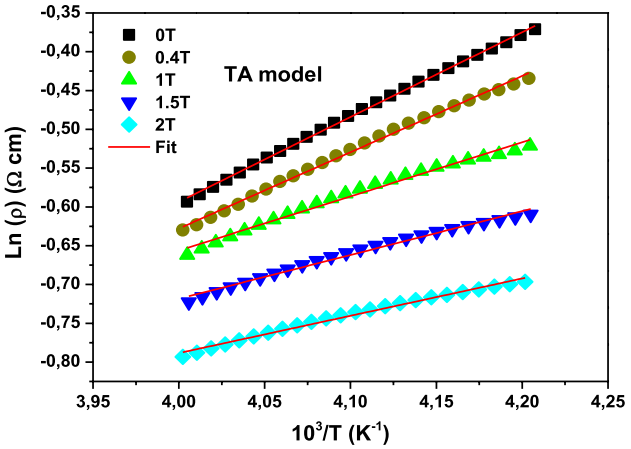

Fig. 10 Fit of high-temperature resistivity data using TA model for LDSMO sample

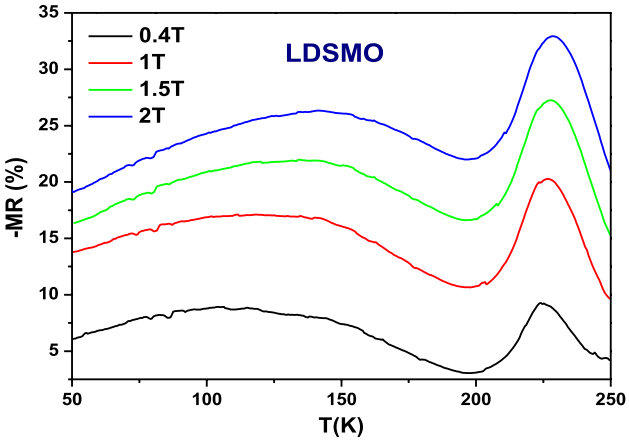

Fig. 11 Temperature dependence of magnetoresistance under several values of applied magnetic field for LDSMO sample

$$\rho = \rho_0 \exp\left(\frac{T_0}{T}\right)^{0.25} \tag{4}$$

where ρ_0 is the Mott residual resistivity and T_0 is the Mott characteristic temperature, given by

$$T_0 = \frac{16\alpha^3}{K_B N(E_F)} \tag{5}$$

where $N(E_F)$ is the density of states and the constant α is taken to be equal to 2.22 nm^{-1} [29]. The value of T_0 is calculated from the slope of the curve $\mathrm{Ln}(\rho) = f(T^{-0.25})$ (Fig. 10). The calculated values of T_0 and $N(E_F)$ are listed in Table 2. Finally, for the TA model where hopping is thermally activated, the mechanism is given by

$$\rho = \rho_0 \exp\left(\frac{E_a}{k_B T}\right) \tag{6}$$

The validity of this model is clear through the linear behavior in the Fig. 10. Also, one can observe a decrease in E_a with increasing the applied magnetic fields. This behavior is attributed to the enhancement of double exchange, leading a delocalization of the charge carriers. Thus, for the previous models, the SPH model seems to be the most suitable to describe resistivity evolution due to the important correlation between experimental and theoretical data (R^2 close to 1).

The evolution of MR as function of temperature, calculated from resistivity data in Fig. 5, is shown in Fig. 11. MR is determined using the following formula:

$$\mathrm{MR}(\%) = \frac{\rho(H) - \rho(0)}{\rho(0)} \times 100 \tag{7}$$

where $\rho(H)$ and $\rho(0)$ are the resistivity values under applied magnetic field $\mu_0 H$ and in zero applied magnetic field, respectively. As seen in Fig. 11, the MR effect appears near 225 K and the maximum of MR increases with the increase of the applied magnetic field due to alignment of Mn spins, which allows the delocalization of e_g electron and the increase of the conductivity of the LDSMO sample. For 2 T applied field, maximum MR reaches 33% near 230 K for LDSMO sample. In fully magnetized ferromagnetic manganites, a negative MR can be observed under a weak field due to spin-dependent charge carrier tunneling across domain walls or grain boundaries [30, 31]. These effects could be relevant in the present manganite sample.

Figure 12 shows the evolution of resistivity as function of magnetic field at different temperatures. The field was isothermally applied from 1 to − 1 T. According to these

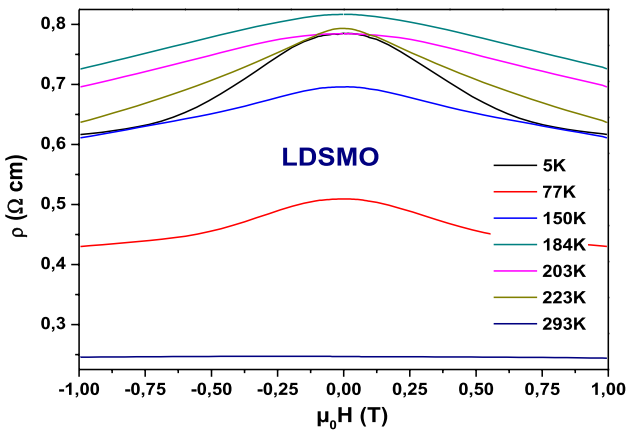

Fig. 12 Magnetic field dependence of electrical resistivity recorded under several values of temperature for LDSMO sample

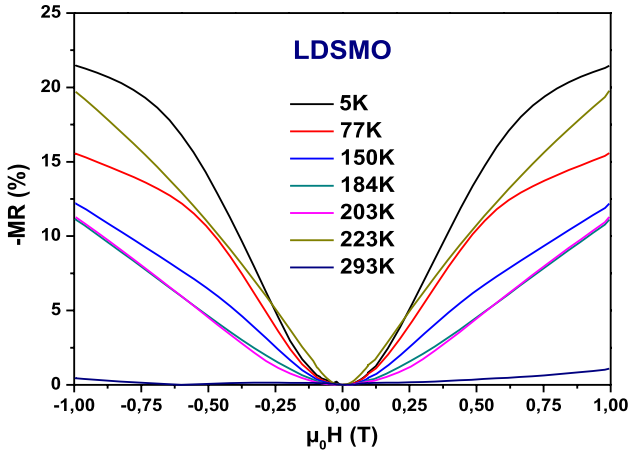

Fig. 13 Magnetic field dependence of isothermal magnetoresistance for LDSMO sample

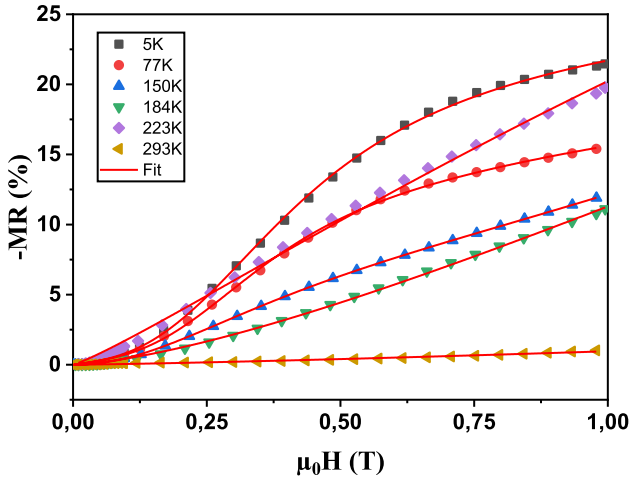

Fig. 14 Experimental (symbols) and theoretical (solid lines) magnetic field dependence of MR for LDSMO sample

curves, resistivity decreases when $|\mu_0 H|$ increases, suggesting the presence of important low-field MR values. To investigate the field-dependent magnetoresistive response of LDSMO compound, evolution of MR as a function of applied magnetic field for different temperatures is shown in Fig. 13. At 5 K and even below 1 T field, a sharp increase of MR is achieved (around 22% for only 1 T applied field). On the other hand, the enhancement in the negative MR value near T_C might be due to spin-polarized tunneling. We have also recorded around 19% of negative MR at T_C for only 1 T applied field. Recently, a new model was established to describe the magnetic field dependence of MR: this model suggests that MR(H) curves can be governed by a universal law that can be described by the following relation [32]:

$$-\mathrm{MR}(\mu_0 H) = \frac{K \times H^{\mathrm{p}}}{H_{\mathrm{L}}^{\mathrm{p}} + H^{\mathrm{p}}} + \frac{(100 - K) \times H^{\mathrm{q}}}{H_{\mathrm{H}}^{\mathrm{q}} + H^{\mathrm{q}}} \tag{8}$$

where K is the amplitude of low-field MR, $\mu_0 H_{\mathrm{L}}$ and $\mu_0 H_{\mathrm{H}}$ are critical field values characterizing low-field and high-field MR, respectively, and p and q are critical exponents characterizing low-field and high-field MR, respectively [32]. We have fitted our MR(H) curves using relation (8) and we have gathered the fitted curves in Fig. 14 and the fitting results are summarized in Table 3. According to Fig. 14, the correspondence between experimental and theoretical results is evident, which supports the validity of this model. According to the results of Table 3, one can observe that the low-field MR amplitude K decreases with increasing temperature and reaches zero near T_ρ. The critical field $\mu_0 H_{\mathrm{H}}$ should exhibit a minimum near T_ρ [32], which is not the case here due to the presence of resistivity peak near T_C (Fig. 5). This fact indicates that the minimum of $\mu_0 H_{\mathrm{H}}$ is directly linked to the metal–insulator transition and supports the extrinsic origin of the resistivity peak recorded in the vicinity of T_ρ.

Table 3 Magnetic field dependence of MR fitting results by using relation (8) for LDSMO sample

T (K)	K (%)	$\mu_0 H_{\mathrm{L}}$ (T)	$\mu_0 H_{\mathrm{H}}$ (T)	p	q
5	19.27	0.422	21.55	2.731	0.953
77	10.60	0.366	14.10	3.031	1.030
150	8.73	0.410	3.90	2.073	2.154
184	0.00	–	4.12	–	1.457
203	0.00	–	3.68	–	1.555
223	0.00	–	3.31	–	1.147
293	0.00	–	38.65	–	1.269

4 Conclusion

We have investigated the effect of dysprosium on the electrical and magnetotransport properties of $La_{0.75}Dy_{0.05}Sr_{0.2}MnO_3$ sample elaborated by sol–gel method. Resistivity measurements versus temperature for several applied magnetic field values were studied in the vicinity of the metal–insulator transition temperature (180 K). For applied magnetic fields below 1 T, the resistivity shows a second peak near T_C, which can be attributed to the competition between the double exchange and super exchange interactions. The magnetotransport in the metallic phase can be described by Zener's polynomial law, while small polaron hopping mechanism is more suitable to describe resistivity in the insulating phase. We have recorded about MR(T) ~ 22% at T_C and about M(H) ~ 19% at T_C, for only

1 T applied field. The important MR values indicate that our sample can be used for magnetic field sensing.

Funding This research did not receive any specific grant from funding agencies in the public, commercial, or not-for-profit sectors.

Compliance with ethical standards

Conflict of interest The authors confirm that there are no known conflicts of interest associated with this publication and there has been no significant support for this work that could have influenced its outcome.

References

1. A. Elghoul, A. Krichene, W. Boujelben, J. Phys. Chem. Solids **98**, 263 (2016)
2. A. Elghoul, A. Krichene, N. Chniba Boudjada, W. Boujelben, Appl. Phys. A **125**, 780 (2019)
3. A. Krichene, W. Boujelben, A. Cheikhrouhou, J. Alloys Compd. **550**, 75 (2013)
4. M. Bourouina, A. Krichene, N. Chniba Boudjada, W. Boujelben, J. Alloys Compd. **680**, 67 (2016)
5. L. Xu, L. Chen, J. Fan, K. Bärner, L. Zhang, Y. Zhu, L. Pi, Y. Zhang, D. Shi, Ceram. Int. **42**, 8234 (2016)
6. MdM Seikh, L. Sudheendra, C.N.R. Rao, J. Solid State Chem. **177**, 3633 (2004)
7. J. Mira, J. Rivas, L.E. Hueso, F. Rivadulla, M.A.L. Quintela, M.A.S. Rodríguez, C.A. Ramos, Phys. Rev. B **65**, 024418 (2001)
8. W. Mabrouki, A. Krichene, N. Chniban Boudjada, W. Boujelben, Appl. Phys. A **126**, 182 (2020)
9. T. Sarkar, B. Ghosh, A.K. Raychaudhuri, T. Chatterji, Phys. Rev. B **77**, 235112 (2008)
10. S.V. Trukhanov, L.S. Lobanovski, M.V. Bushinsky, I.O. Troyanchuk, H. Szymczak, J. Phys. Condens. Matter **15**, 1783 (2003)
11. K.H. Kim, M. Uehara, C. Hess, P.A. Sharma, S.W. Cheong, Phys. Rev. Lett. **84**, 2961 (2000)
12. E. Dagotto, T. Hotta, A. Moreo, Phys. Rep. **344**, 1 (2001)
13. N.A. Babushkina, L.M. Belova, D.I. Khomskii, K.I. Kugel, O.Y. Gorbenko, A.R. Kaul, Phys. Rev. B **59**, 6994 (1999)
14. A. Krichene, M. Bourouina, D. Venkateshwarlu, P.S. Solanki, S. Rayaprol, V. Ganesan, W. Boujelben, D.G. Kuberkar, J. Magn. Magn. Mater. **408**, 116 (2016)
15. A. Elghoul, A. Krichene, N. Chniba Boudjada, W. Boujelben, Ceram. Int. **44**, 12723 (2018)
16. A. Elghoul, A. Krichene, N. Chniba Boudjada, W. Boujelben, Ceram. Int. **44**, 14510 (2018)
17. A. Krichene, W. Boujelben, S. Mukherjee, P.S. Solanki, N.A. Shah, Acta Mater. **131**, 491 (2017)
18. P.D. Tejaswini, M.D. Babu, Daivajna, Thrupthi. J. Alloys Compd. **741**, 97 (2018)
19. A. Modi, M.A. Bhat, D.K. Pandey, S. Bhattacharya, N.K. Gaur, G.S. Okram, J. Magn. Magn. Mater. **424**, 459 (2017)
20. A. Barnabé, F. Millange, A. Maignan, M. Hervieu, B. Raveau, Chem. Mater. **10**, 252 (1998)
21. N. Panwar, D.K. Pandya, S.K. Agarwal, J. Phys. Condens. Matter **19**, 456224 (2007)
22. R. Ang, Y.P. Sun, J. Yang, X.B. Zhu, W.H. Song, J. Appl. Phys. **100**, 073706 (2006)
23. A. Krichene, W. Boujelben, S. Mukherjee, N.A. Shah, P.S. Solanki, J. Phys. Chem. Solids **114**, 21 (2018)
24. A. Krichene, P.S. Solanki, D. Venkateshwarlu, S. Royaprol, V. Ganesan, W. Boujelben, D.G. Kuberkar, J. Magn. Magn. Mater. **381**, 470 (2015)
25. D. Varshney, N. Dodiya, M.W. Shaikh, J. Alloys Compd. **509**, 7447 (2011)
26. A. Krichene, W. Boujelben, S. Mukherjee, N.A. Shah, P.S. Solanki, Phys. Chem. Chem. Phys. **20**, 12608 (2018)
27. B. Munirathinam, M. Krishnaiah, U. Devarajan, S.E. Muthu, S. Arumugam, J. Phys. Chem. Solids **73**, 925 (2012)
28. R. Jia, D. Deng, P. He, Y. Xu, Z. Feng, Y. Liu, S. Cao, J. Zhang, J. Magn. Magn. Mater. **329**, 65 (2013)
29. W.H. Jung, Sci. Lett. **190**, 1653 (2000)
30. R. Mahesh, R. Mahendiran, A.K. Raychaudhuri, C.N.R. Rao, Appl. Phys. Lett. **68**, 2291 (1996)
31. H.Y. Hwang, S.W. Cheong, N.P. Ong, B. Batlogg, Phys. Rev. Lett. **77**, 2041 (1996)
32. A. Krichene, W. Boujelben, N.A. Shah, P.S. Solanki, J. Alloy. Compd. **820**, 153400 (2020)